DOI: 10.1002/smll.200800897

Magnetic Imaging of Cyanide-Bridged Co-ordination Nanoparticles Grafted on FIB-Patterned Si Substrates

Alberto Ghirri, Andrea Candini, Marco Evangelisti, Gian Carlo Gazzadi, Florence Volatron, Benoit Fleury, Laure Catala, Christophe David, Talal Mallah, and Marco Affronte*

***P**russian blue CsNiCr nanoparticles are used to decorate selected portions of a Si substrate. For successful grafting to take place, the Si surface needs first to be chemically functionalized. Low-dose focused ion beam patterning on uniformly functionalized surfaces selects those portions that will not participate in the grafting process. Step-by-step control is assured by atomic force and high-resolution scanning electron microscopy, revealing a submonolayer distribution of the grafted nanoparticles. By novel scanning Hall-probe microscopy, an in-depth investigation of the magnetic response of the nanoparticles to varying temperature and applied magnetic field is provided. The magnetic images acquired suggest that low-temperature canted ferromagnetism is found in the grafted nanoparticles, similar to what is observed in the equivalent bulk material.*

Keywords:
- magnetic nanoparticles
- molecular magnets
- nanolithography
- scanning probe microscopy
- self-assembled monolayers

1. Introduction

Molecular nanomagnets (MNMs) have recently shown great potential for applications in magnetic data storage and processing. A fundamental requirement for the exploitation of their functionalities at the nanoscale is the capability to deposit these objects on surfaces. Important progress has been made in the surface grafting of Mn_{12} molecules[1–4] as well as other molecular systems such as self-assembled terbium-phtalocyanine,[5] Cr_7Ni,[6] and Mn_6[7] clusters. A second requirement is the positioning of the molecules onto selective portions of the substrate. Along these lines, several chemical and physical approaches are under investigation such as micro-contact printing,[8–10] photolithography,[11] self-assembly by water-droplet templates,[12] local oxidation nanolithography,[13] and deposition on prepatterned substrate.[14] Selective grafting of isolated molecules onto nanopatterned surfaces has been reported.[13] Current interest is in procedures that combine top-down with bottom-up methods, for example lithography together with the functionalization of either substrates or molecules.[15]

The $Cs_{0.7}Ni[Cr(CN)_6]_{0.9}$ Prussian blue analog, hereafter (CsNiCr)–PBA, is a molecule-based compound exhibiting long-range ferromagnetic order below $T_C = 70\,K$.[16] Recently (CsNiCr)–PBA has been stabilized in the form of nanoparticles with <6-nm diameter.[17,18] In what follows, we report a method that combines chemistry[19] with focused ion beam (FIB) direct lithography,[21] allowing for selective grafting of the (CsNiCr)–PBA nanoparticles on multiple scales. The central characteristic of this multistep approach is the use of FIB lithography, whose physical sputtering-based patterning is fully compatible with the functionalization chemistry. The

[*] Dr. A. Ghirri, Prof. M. Affronte
CNR-INFM National Research Center on nanoStructures and bioSystems at Surfaces (S^3) and
Dipartimento di Fisica, Università di Modena e Reggio Emilia, via Campi 213/a, 41100 Modena (Italy)
E-mail: alberto.ghirri@unimore.it

Dr. A. Candini, Dr. M. Evangelisti, Dr. G. C. Gazzadi
CNR-INFM National Research Center on nanoStructures and bioSystems at Surfaces (S^3)
via Campi 213/a, 41100 Modena (Italy)

F. Volatron, Dr. B. Fleury, Dr. L. Catala, Prof. T. Mallah
ICMMO-Equipe Chimie Inorganique
Université Paris-Sud
91405 Orsay (France)

Dr. C. David
Laboratoire de Photonique et de Nanostructures
CNRS, route de Nozay
91460 Marcoussis (France)

Supporting Information is available on the WWW under http://www.small-journal.com or from the author.

small NANO MICRO

central characteristic of this multistep approach is the use of FIB machining, which allows direct lithography in a single step. The low-dose patterning of just the functionalized overlays with respect to the deep grooving of the substrate underneath[14] has the advantage of avoiding dramatic modification of the superficial morphology.

In spite of the work done on the positioning of MNMs on surfaces, the magnetic characterization of the resulting coatings — albeit crucial — is still lacking, both because of technical difficulties (low temperatures and small magnetic fields are required) and the relatively low magnetization of the nanoobjects. Scanning Hall probe microscopy (SHPM) is a powerful technique that directly probes the magnetic stray fields at surfaces. In contrast to magnetic force microscopy, SHPM is a non-invasive tool that can be employed in a wide range of temperatures (down to — and even below — liquid-helium temperature) and magnetic fields (up to several Tesla). Seminal SHPM investigations have been reported for magnetic domains in metal and oxides,[20,22] and vortices in superconductors.[23] Here we employ SHPM to describe for the first time the magnetic features of a molecule-based monolayer for varying temperatures and applied magnetic fields.

2. Results and Discussion

2.1. Fabrication of the Patterned Monolayer

The grafting of the PBA nanoparticles on the silicon surface is carried out using a three-step procedure:[19] i) functionalization of an H-terminated Si(100) substrate by undecanoic acid following a well-known method,[24] ii) modification of the acid terminated substrate to obtain a dangling tridentate ligand that is able to chelate a $Ni^{(II)}$ metal ion, and iii) simple immersion of the substrate in an aqueous solution containing the nanoparticles to obtain the grafted monolayer (see Section 4).

Between steps (ii) and (iii), we use FIB patterning to remove the organic ligand from selected regions of the substrate (Figure 1). We employ an FIB-scanning electron microscopy (SEM) dual beam system, enabling us to monitor ion-beam processing with simultaneous SEM imaging. The FIB column is equipped with a Ga^+ source and operated at 30 keV with a 7 nA beam current. To remove the organic layer we use a low-dose irradiation (1.3×10^{16} ions cm^{-2}), in order to avoid milling the substrate. Then, we rinse the sample with methanol and graft PBA nanoparticles from the liquid phase (step [iii]). This approach is straightforward because FIB allows for high-resolution direct lithography in a single step.

Figure 2a shows the result of the FIB patterning, which provided irradiated stripes 2 μm wide (dark region) alternated with nonirradiated stripes 5 μm wide (light gray). The patterning of 100-nm-wide stripes and circular dots with 2-μm diameter is also reported in the Supporting Information, in order to demonstrate the feasibility of this technique for obtaining arbitrary shapes with nanoscale resolution. The

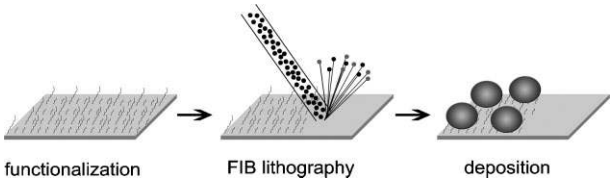

Figure 1. Schematic drawing showing the fabrication procedure. Upon the functionalization of the Si(100) surface, portions of ligand are removed by the FIB patterning. The sample is then rinsed with methanol to wash off the debris of the sputtering process. In the last step, the deposition is carried out by submerging the sample in the solution of (CsNiCr)–PBA nanoparticles.

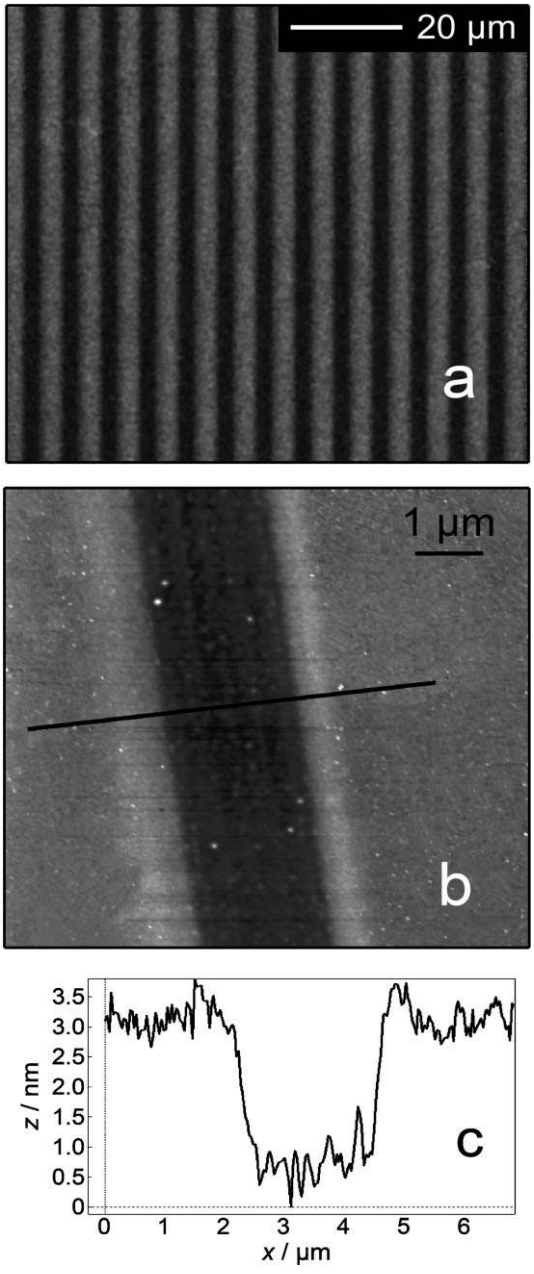

Figure 2. a) SEM micrograph showing the patterning of the surface before the deposition of the nanoparticles: light gray stripes are nonirradiated whilst the darker ones were irradiated by the ion-beam. b) AFM image focalized on one irradiated stripe. c) AFM profile taken along the reference line in (b): the 3 nm step shows the groove in the organic layer made by FIB.

atomic force microscopy (AFM) image in Figure 2b shows a 3-nm deep groove, whose profile (Figure 2c) marks the contours between the irradiated and nonirradiated areas, thus confirming the removal of the organic ligand in the irradiated regions.

After step (iii), that is, the grafting of nanoparticles, we investigate the sample by means of SEM (Figure 3) and AFM (Figure 4). The SEM micrograph of Figure 3a shows an area between an irradiated and a nonirradiated stripe. The image clearly shows that the nanoparticles graft solely onto the nonirradiated region. To enhance the topographic contrast the sample is tilted by 52° with respect to the electron beam. The image is taken using a primary beam of 15 keV in ultrahigh resolution (UHR) mode, operating with an immersion field and a through-the-lens detector (TLD). A high-resolution (10^6 magnification) SEM micrograph (Figure 3b) shows a density of $<8 \times 10^4$ particles per μm^2. We note that their shape is prolate in most cases, in agreement with transmission electron microscope measurements.[18] To estimate their dimension, we measure the size of more than 200 particles along the horizontal direction of Figure 3b. The resulting data map onto a Gaussian distribution (Figure 3c) with mean value $l^* = (8.0 \pm 2.0)$ nm and standard deviation $\delta = 4.6$ nm.

AFM images in Figure 4 are taken on a) irradiated and b) nonirradiated area. The striking difference between the topographic contrast in the two regions clearly evidences the selective deposition of the (CsNiCr)–PBA nanoparticles. The average height of Figure 4b is about 6 nm, suggesting monolayer deposition, whereas the dimension of the grafted particles is in agreement with the SEM images (Figure 3b). Therefore, we can confidently consider the height of the individual nanoparticle to be ≈6 nm and, because of their mean largeness l^*, we calculate the particle volume $V = 384\ nm^3$.

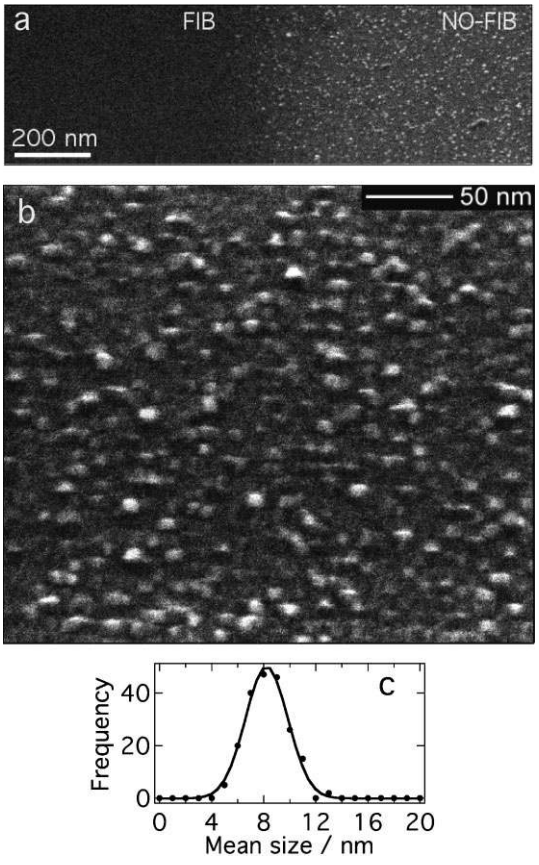

Figure 3. SEM imaging of the patterned monolayer. a) Micrograph demonstrating how particles graft solely onto the nonirradiated areas. b) High-resolution SEM image of (CsNiCr)–PBA nanoparticles deposited on unpatterned area. c) Gaussian distribution of the sizes of the particles with mean value $l^* = 8.0 \pm 2.0$ nm and standard deviation $\delta = 4.6$ nm.

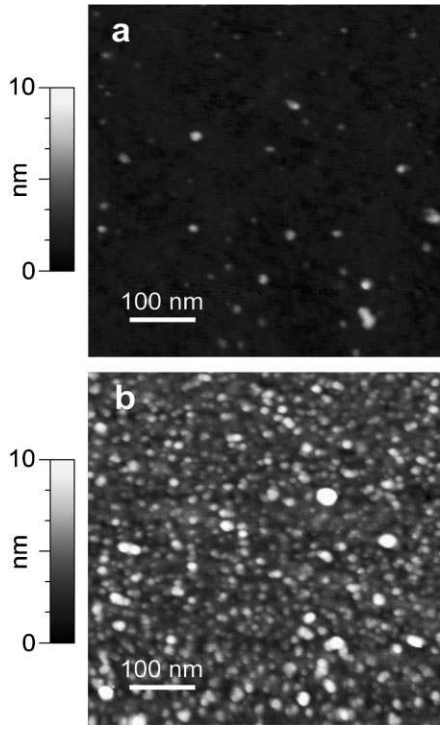

Figure 4. AFM images taken on the a) irradiated and b) nonirradiated area, demonstrating how particles graft solely onto the nonirradiated areas.

The attenuated total reflection infrared (ATR-FITR) spectrum of the as-grafted particles presents two bands in the 2000–2200 cm^{-1} region (Figure 5). The band at 2172 cm^{-1} corresponds to the bridging cyanide ligands as expected for the (CsNiCr)–PBA nanoparticles. The large band at 2100 cm^{-1} is due to the remaining Si–H bonds of the hydrogenated Si(100) surface. The presence of such a band indicates the absence of oxidation processes during the different steps. It is noteworthy that washing the substrate several times with water leads first to a slight decrease of the intensity of the cyanide bridging

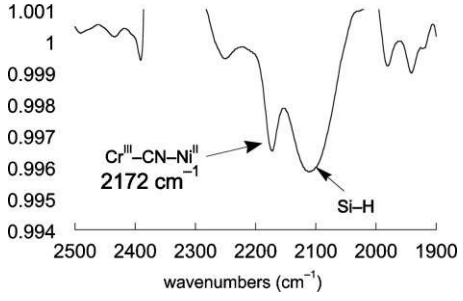

Figure 5. ATR FTIR spectrum of a monolayer of the (CsNiCr)–PBA nanoparticles on functionalized Si(100).

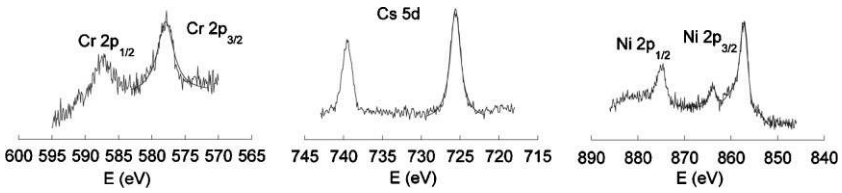

Figure 6. XPS spectra of the monolayer of (CsNiCr)–PBA nanoparticles taken at the Cr, Cs, and Ni edges.

band in comparison to that of Si–H. Repeating the washing procedure several times leads to a stabilization of the bands intensity (only extensive sonication in water for at least half an hour leads to a decrease of the cyanide-bridged band intensity). These observations indicate that physisorbed particles are first removed upon rinsing with water while the remaining particles interact more strongly with the functionalized surface. Reasonably, one may consider that these strongly interacting particles form a single monolayer. In order to ensure the integrity of the particles after the grafting process, X-ray photoelectron spectroscopy (XPS) was performed at the Ni and Cr 3p edge and the Cs 5d edge. The spectra (Figure 6) show the expected characteristics for the different edges.[25] The analysis of the relative intensities of the three elements leads to the elemental ratio: Cr/Ni = 0.9 and Cs/Ni = 0.66, as expected from the unit formula of the nanoparticles: $Cs_{0.7}Ni[Cr(CN)_6]_{0.9}$.[17]

2.2. Magnetic Characterization of the Nanoparticles in Polymeric Matrix

At temperatures much lower than $T_C \approx 70$ K, each particle develops its own magnetic moment and can thus be treated within the frame of super-paramagnetism. Considering the mean size of the ferromagnetic particles, we estimate their magnetic moment to be as large as 2000 μ_B. Figure 7 shows the out-of-phase susceptibility χ'' of the nanoparticles embedded in a polymeric matrix of polyvinylpyrrolidone (PVP), prior to grafting By changing the amount of PVP, we control the degree of the dilution, which eventually modifies the strength of the interaction between the particles. Particularly, the data in Figure 7 refer to a ≈10% dilution, that is, only one-tenth of the sample weight is constituted by particles. The strongly

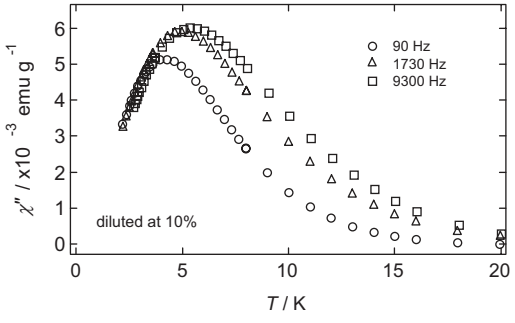

Figure 7. Temperature dependence of the out-of-phase susceptibility at different ac-frequencies, as labeled, for a 10% dilution of nanoparticles embedded in PVP.

frequency-dependent nonzero χ'', as the one in Figure 7, is associated with super-paramagnetism. The shell of organic ligands surrounding the metal cores prevents clustering of the particles and direct magnetic exchange between them. However, dipolar interactions can still be large, especially considering the very large magnetic moment carried by each particle. This is neatly the case for the particles in Figure 7. Indeed, the slowing of the dynamics at the lowest temperatures (χ'' is insensitive to the frequency change below ≈4 K), and the frequency-dependence of the maximum absorption are known to be related to interparticle interactions.[26] We mention that not even dilutions as small as 1% are sufficient to suppress the onset of these correlations, although they are notably weakened. In view of these results, we expect the dipolar interactions to be significantly large for the particles grafted onto the Si surface.

2.3. Magnetic Characterization of the Nanoparticles at Surface

For magnetically investigating patterned monolayers, we use a scanning Hall probe microscope (NanoMagnetics Instruments) inserted in a cryo-magnetic system (Quantum Design PPMS) working down to $T = 2$ K and in magnetic fields up $H = 70$ kOe. A gold pad, working as a tunneling tip, is close to the Hall sensor on the same head and provides the necessary feedback for approaching and scanning the probe (see Supporting Information). Thus, topographic (by STM) and magnetic (by Hall probe) images can be taken simultaneously. Highly doped Si substrate is used in order to maintain the tunneling operative down to the lowest temperature. The sample is mounted as sketched in Figure 8a on the cryogenic insert.

A first set of images of the grafted nanoparticles is obtained at $T = 100$ K, i.e., above the ferromagnetic ordering temperature $T_C = 70$ K of (CsNiCr)–PBA. The oblique stripes detected by STM imaging (Figure 8b) represent a portion of the patterned texture. Simultaneously, we collect magnetic images by SHPM. At fields as high as $H = +70$ kOe, the magnetic profile depicted in Figure 8c shows oblique stripes with the same orientation and pitch as in the STM image. Note that a color scale is employed to show the intensity of the stray field component B_{sf}^z perpendicular to the Hall probe. Upon switching the applied field to the opposite $H = -70$ kOe value, we observe the reversal of the magnetic profile in Figure 8d in which the red (blue) scale is used for positive (negative) fields. This confirms the true (para)magnetic origin of the stripes, whose color get more intense along the direction of the applied field. The SHPM images taken on the substrate before the deposition of (CsNiCr)–PBA nanoparticles, evidence that the Ni^{2+}–ligand complex belonging to the layer provides no relevant contribution to the signal of Figure 8c and d.

For $T = 20\,\text{K} \ll T_C$, we collect a representative series of pictures (Figure 9) of the grafted nanoparticles on a scan area of $7 \times 7\ \mu m^2$, with the tip in the lift mode (i.e., with no feedback and at fixed height $h = 350$ nm from the surface).[27] Specifi-

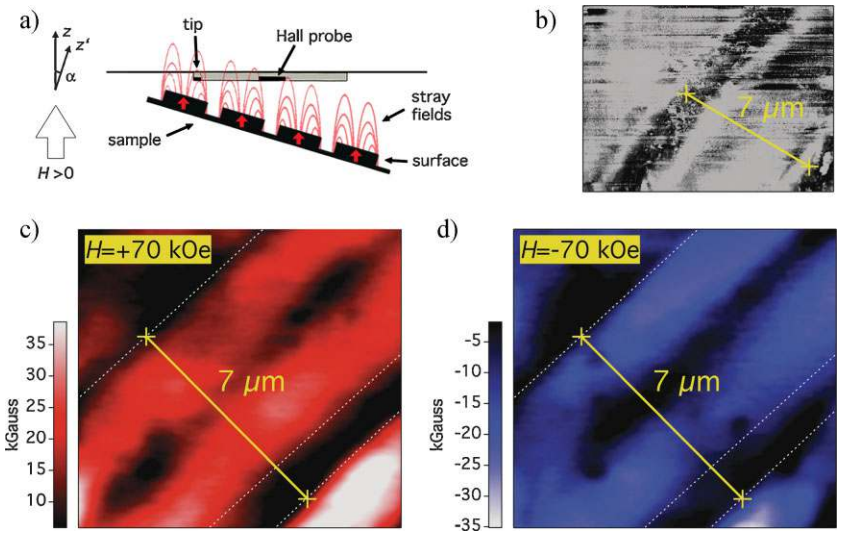

Figure 8. a) Experimental set-up of the SHPM illustrating the disposal of sample, scanning head and magnetic fields. b) STM image taken at $T = 100$ K showing the patterning of the surface. c) Magnetic image taken at $T = 100$ K simultaneously with (b) and with an applied-field $H = +70$ kOe. The color scale indicates the strength of the detected stray field. The zero-field value of the scale is set to an arbitrary baseline. d) Same as (c) but with reversed field ($H = -70$ kOe): notice that the color scale is reversed while the same spots are observed.

The topographic studies suggest that the particles are elongated along the planar surface. A particle shape anisotropy thus promotes a hard axis of magnetization perpendicularly to the surface. As a consequence, the dipolar field arising from interparticle correlations should lie in the plane. We point out that, in view of the very large magnetic moment per particle and the relatively high surface coverage, the dipolar field is significantly large (Figure 8). At zero applied field one would therefore expect the presence of magnetic domains uncorrelated with respect to the patterned texture, as indeed observed in Figure 9h. As the applied field is increased, both the anisotropy and the dipolar field are overcome, and the magnetic moments of the nanoparticles tend to align along the magnetic field direction. In this situation, strong stray fields are detected solely in the nonirradiated stripes (i.e., where the particles are present).

To get more details on the stray fields across the patterned texture, we take images in tunneling mode, so that the Hall sensor is closer to the surface ($h = 250$ nm). Figure 10a and b magnify a limited area, in which we draw a line across an individual stripe as a guide to the eyes. For both images, we employ an applied-field of $H = +10$ kOe. The image (a) collected at $T = 100$ K neatly shows that larger magnetic intensities are obtained approaching the border from both sides. This changes once we cool down to $T = 20$ K, as depicted in Figure 10b. One can notice that the symmetry is now lost and the largest signal is achieved on one side only. The experimental magnetic profiles along the reference lines are depicted in Figure 10c and d. The peculiarities in their magnetic profiles can be qualitatively explained by simple micromagnetic calculations, for which we assume the stripes to be magnetically uniform. This approximation is justified by the relatively large density of particles grafted on the surface. Figure 10e and f show the calculated results of the magnetic profiles sectioned along the lines depicted in the experimental images. For $T = 100$ K, we consider an out-of-plane magne-

cally, a hysteresis-type cycle is performed by varying the applied field within $H = \pm 10$ kOe. Figure 9a shows, for comparison, the hysteresis loop of (CsNiCr)–PBA particles when measured by conventional magnetometry on a massive powder specimen at 20 K. We first note that, for the same conditions of height and H, the color scales in Figure 9b–n indicate stronger stray fields than that observed for $T = 100$ K, because of the ferromagnetic transition. Although the contours are relatively smooth because of the height of the Hall probe from the sample, the main magnetic features are evident. Oblique stripes are neatly visible for $H > +1$ kOe (b–d). As H vanishes (e–g) down to $H = 0$ (h), magnetic spots appear, suggesting the presence of random magnetic domains. At negative fields, the spots rearrange themselves (i–k) to again obtain the stripe-like shape for $H < -1$ kOe (l–n), though with opposite direction with respect to positive H. For $|H| > 1$ kOe the intensity of the stray field increases without significant modification of the image.

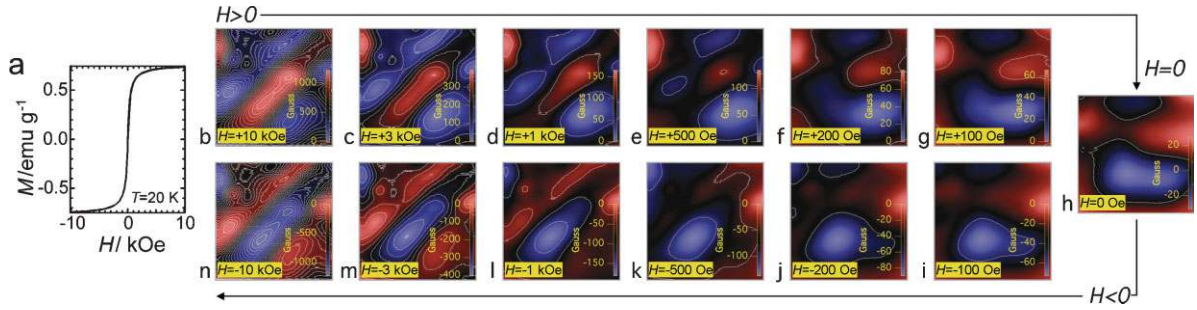

Figure 9. a) Magnetization curve M versus H taken on a powder sample of (CsNiCr)–PBA nanoparticles. b–n) Applied-field evolution of the magnetic domains of the particles grafted on pattened substract. These images were collected at $T = 20$ K with the tip in the lift mode ($h = 350$ nm). The scan area is $7 \times 7\ \mu m^2$.

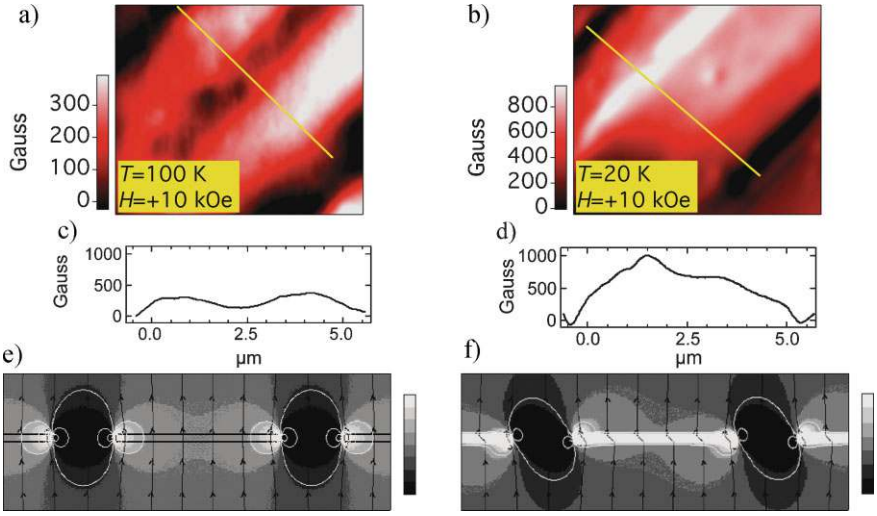

Figure 10. Comparison between magnetic images taken on the same area but collected at a) $T = 100$ K and b) $T = 20$ K, with an applied field $H = +10$ kOe. c) and d) experimental profiles of the stray field taken across the reference lines depicted in (a) and (b), respectively. e) and f) pictorial simulations of the magnetic profiles sectioned along the respective reference lines in (a) and (b), respectively.

tization M_n of the stripe, which develops along the applied-field direction. As can be seen, we reproduce well the symmetry of the border effect. For $T = 20$ K, we need to introduce an additional in-plane component M_t of the magnetization of the stripe, for which we assume $|M_n|/|M_t| = 1.9$. The result closely resembles the experimental behavior. The origin of the two magnetization components at low temperature should likely be associated with a canting of the Ni and Cr sublattices in the ordered phase, whose onset was already detected by magnetization measurements on the bulk equivalent material.[28]

3. Conclusions

We have developed a hybrid procedure that combines liquid phase grafting with direct FIB patterning, by which we are able to deposit $Cs_{0.7}Ni[Cr(CN)_6]_{0.9}$ cyanide-bridged coordination nanoparticles on selected portions of Si surfaces. The success of our procedure is demonstrated by locally probing the magnetic properties employing SHPM. The dependency of the magnetic images on the temperature and applied field suggests that the bulk equivalent material constituting the nanoparticles comprises two canted magnetic sublattices in its ordered phase. This is one of the first reports on direct magnetic measurements for monolayers of molecular nanomagnets, and proves the potentialities of the SHPM technique for studying such systems.

4. Experimental Section

We used P-boron doped silicon substrates (resistivity $<0.02\ \Omega$cm). The coupling of the tridentate organic ligand to the acid terminated surface (described in Ref. [24]) was carried out by immersing the Si wafer functionalized with undecanoic acid for 5 min in a distilled dichloromethane solution containing the coupling agent EDC [*N*′-(3-dimethylaminopropyl)-*N*-ethyl-carbodiimide hydrochloride], then 10 mg of the organic ligand *N*,*N*-bis[(pyridin-2-yl)methyl]propane-1,3-diamine[29] were added to the solution. The NH_2 amine group reacted with the acic group of the substrate in the presence of the coupling agent for 14 h at room temperature under Ar. Then the wafer was removed from the solution, rinsed with dichloromethane, isopropanol, and dichloromethane. It was then dried under vacuum. The dry wafer, freshly functionalized with the tridentate organic ligand, was immersed in a distilled methanolic solution containing $Ni(H_2O)_6Cl_2$ for 15 min under Ar. The wafer was then removed, rinsed thoroughly with methanol, sonicated in methanol for 30 s, and then dried under vacuum. The synthesis of the nanoparticles was carried out as described elsewhere.[17]

FIB patterning and SEM imaging were performed in a dual beam system (FEI Strata DB235M) at CNR-INFM S3, combining a Ga^+ ion column and a field-emission electron column with nominal resolutions of 6 and 2 nm, respectively. The dual beam configuration enabled to monitor ion beam processing with simultaneous SEM imaging. FIB was operated at 30 keV, 7 nA beam current and low dose ion irradiation (1.3×10^{16} ions cm^{-2}), to remove the organic layer only, without milling the substrate. SEM imaging was performed with 15 keV beam energy in UHR mode, operating with immersion field lens and TLD electron detection. To enhance topographic contrast the sample was tilted by 52° with respect to the electron beam.

AFM images were carried out at Université Paris-Sud using a Veeco Nanoscope III microscope working in tapping mode at a frequency of 1 Hz with an ultra-sharp tip.

SHPM experiments were performed at CNR-INFM S^3 by means of a Nanomagnetics Inc. LT-SHPM microscope and Quantum Design PPMS cryo-magnetic setup. We employed commercial Hall sensors (Nanomagnetics Instruments Inc.) made by crosses on GaAs/AlGaAs patterned heterostructures (see Supporting Information).

Magnetization data were taken on bulk specimens of (CsNiCr)–PBA nanoparticles embedded in matrix of PVP. Magnetometry experiments were performed at CNR-INFM S^3 by means of a Quantum Design Physical Properties Measurements System and dc-extraction technique.

Acknowledgements

This work was carried out within the framework of the EU Network of Excellence "MAGMANet" contract N. 515767 and supported by the PRIN N. 2006029518 of Italian Ministry of

Research. We aknowledge the Région Ile-de-France in the framework of C'Nano IdF. C'Nano-IdF is the nanoscience competence center of Paris Region, supported by CNRS, CEA, MESR, and Région Ile-de France.

[1] D. Ruiz-Molina, M. Mas-Torrent, J. Gómez, A. I. Balana, N. Domingo, J. Tejada, M. T. Martínez, C. Rovira, J. Veciana, *Adv. Mater.* **2003**, *15*, 42.
[2] B. Fleury, L. Catala, V. Huc, C. David, W. Z. Zhong, P. Jegou, L. Baraton, S. Palacin, P.-A. Albouy, T. Mallah, *Chem. Commun.* **2005**, 2020.
[3] E. Coronado, A. Forment-Aliaga, F. M. Romero, V. Corradini, R. Biagi, V. de Renzi, A. Gambardella, U. del Pennino, *Inorg. Chem.* **2005**, *44*, 7693.
[4] Z. Salman, K. H. Chow, R. I. Miller, A. Morello, T. J. Parolin, M. D. Hossain, T. A. Keeler, C. P. D. Levy, W. A. MacFarlane, G. D. Morris, H. Saadaoui, D. Wand, R. Sessoli, G. G. Condorelli, R. F. Kiefl, *Nano Lett.* **2007**, *7*, 1551.
[5] J. Gómez-Segura, I. Díez-Pérez, N. Ishikawa, M. Nakano, J. Veciana, D. Ruiz-Molina, *Chem. Commun.* **2006**, 1.
[6] V. Corradini, R. Biagi, U. del Pennino, V. de Renzi, A. Gambardella, M. Affronte, C. Muryn, G. Timco, R. E. P. Winpenny, *Inorg. Chem.* **2007**, *46*, 4968.
[7] F. Moro, V. Corradini, M. Evangelisti, V. De Renzi, R. Biagi, U. del Pennino, C. J. Milios, L. F. Jones, E. K. Brechin, *J. Phys. Chem. B* **2008**, *112*, 9729.
[8] M. Cavallini, F. Biscarini, J. Gomez-Segura, D. Ruiz, J. Veciana, *Nano Lett.* **2003**, *3*, 1527.
[9] M. Cavallini, J. Gomez-Segura, D. Ruiz-Molina, M. Massi, C. Albonetti, C. Rovira, J. Veciana, F. Biscarini, *Angew. Chem, Int. Ed.* **2005**, *44*, 888.
[10] M. Mannini, D. Bonacchi, L. Zobbi, F. M. Piras, E. A. Speets, A. Caneschi, A. Cornia, A. Magnani, B. J. Ravoo, D. N. Reinhoudt, R. Sessoli, D. Gatteschi, *Nano Lett.* **2005**, *5*, 1435.
[11] K. Kim, M. Seo, J. Means, V. Meenakshi, W. Teizer, H. Zhao, K. R. Dunbar, *Appl. Phys. Lett.* **2004**, *85*, 3872.
[12] J. Gómez-Segura, O. Kazakova, J. Davies, P. Josephs-Franks, J. Veciana, D. Ruiz-Molina, *Chem. Commun.* **2005**, 5615.
[13] R. V. Martínez, F. García, R. García, E. Coronado, A. Forment-Aliaga, F. M. Romero, S. Tatay, *Adv. Mater.* **2007**, *19*, 291.
[14] V. Corradini, U. del Pennino, R. Biagi, V. de Renzi, A. Gambardella, G. C. Gazzadi, A. Candini, L. Zobbi, A. Cornia, *Surf. Sci.* **2007**, *601*, 2618.
[15] G. Molnár, S. Cobo, J. A. Real, F. Carcenac, E. Daran, C. Vieu, A. Bousseksou, *Adv. Mater.* **2007**, *19*, 2163.
[16] a) E. Manuel, M. Evangelisti, M. Affronte, M. Okubo, C. Train, M. Verdaguer, *Phys. Rev. B* **2006**, *73*, 172406; b) M. Evangelisti, E. Manuel, M. Affronte, M. Okubo, C. Train, M. Verdaguer, *J. Magn. Magn. Mater.* **2007**, *316*, e569.
[17] L. Catala, A. Gloter, O. Stephan, G. Rogez, T. Mallah, *Chem. Commun.* **2006**, 1018.
[18] D. Brinzei, L. Catala, N. Louvain, G. Rogez, O. Stephan, A. Gloter, T. Mallah, *J. Mater. Chem.* **2006**, *16*, 2593.
[19] B. Fleury, F. Volatron, L. Catala, D. Brinzei, E. Rivière, V. Huc, C. David, F. Miserque, G. Rogez, L. Baraton, S. Palacin, T. Mallah, *Inorg. Chem.* **2008**, *47*, 1898.
[20] T. Fukumura, H. Sugawara, T. Hasegawa, K. Tanaka, H. Sakaki, T. Kimura, Y. Tokura, *Science* **1999**, *284*, 1969.
[21] a) G. C. Gazzadi, A. Angeli, P. Facci, S. Frabboni, *Appl. Phys. Lett.* **2006**, *89*, 173112; b) A. Candini, G. C. Gazzadi, A. di Bona, M. Affronte, D. Ercolani, G. Biasiol, L. Sorba, *Nanotechnology* **2006**, *17*, 2105.
[22] J. S. Neal, H. G. Roberts, M. R. Connolly, S. Crampin, S. J. Bending, G. Wastlbauer, J. A. C. Bland, *Ultramicroscopy* **2006**, *106*, 614.
[23] A. Oral, J. C. Barnard, S. J. Bending, I. I. Kaya, S. Ooi, T. Tamegai, M. Henini, *Phys. Rev. Lett.* **1998**, *80*, 3610.
[24] M. R. Linford, C. E. D. Chidsey, *J. Am. Chem. Soc.* **1993**, *115*, 12631.
[25] J. F. Watts, J. Wolstenholme, *An Intoduction to Surface Analysis by XPS and AES*, John Wiley, England 2003.
[26] T. Jonsson, P. Nordblad, P. Svedlindh, *Phys. Rev. B* **1998**, *57*, 497.
[27] We chose the working temperature of $T = 20$ K because i) it is well below T_C and ii) the width of the scan area (7×7 μm^2) is sufficiently large to look at the patterning. At much lower temperatures, for example 2 K, the experimental magnetic images cover areas not larger than 4.5×4.5 μm^2. For instance, the supplementary material provides an image of an area existing within a single stripe for $T = 2$ K.
[28] For applied fields not exceeding 70 kOe, powder samples of the bulk equivalent material show molar magnetization values that are roughly 12% smaller than that expected for full ferromagnetic coupling of all Ni and Cr ions.[16] This discrepancy can be accounted for by a canting angle of $\approx 60^\circ$ between the two ferromagnetic Ni and Cr sublattices. This is likely the result of an intense exchange anisotropy acting on the metal ions. Using $z = 6$ for the number of nearest neighbors and $J/k_B = 6.5$ K for the Ni–Cr exchange strength,[16] a rough mean-field calculation tells us that the exchange field acting on the Ni and Cr ions amounts to $H_{ex} = (2zJ/k_b)S/g\mu_B = 390$ and 530 kOe for Ni and Cr, respectively.
[29] G. S. Matouzenko, A. Bousseksou, S. Lecocq, P. J. van Koningsbruggen, M. Perrin, O. Kahn, A. Collet, *Inorg. Chem.* **1997**, *36*, 5869.

Received: June 25, 2008

